JCB Journal of Cell Biology

REPORT

Myeloid-derived growth factor regulates neutrophil motility in interstitial tissue damage

Ruth A. Houseright[1*], Veronika Miskolci[1*], Oscar Mulvaney[2], Valeriu Bortnov[3], Deane F. Mosher[3], Julie Rindy[2], David A. Bennin[2], and Anna Huttenlocher[1,2]

Neutrophil recruitment to tissue damage is essential for host defense but can also impede tissue repair. The cues that differentially regulate neutrophil responses to tissue damage and infection remain unclear. Here, we report that the paracrine factor myeloid-derived growth factor (MYDGF) is induced by tissue damage and regulates neutrophil motility to damaged, but not infected, tissues in zebrafish larvae. Depletion of MYDGF impairs wound healing, and this phenotype is rescued by depleting neutrophils. Live imaging and photoconversion reveal impaired neutrophil reverse migration and inflammation resolution in *mydgf* mutants. We found that persistent neutrophil inflammation in tissues of *mydgf* mutants was dependent on the HIF-1α pathway. Taken together, our data suggest that MYDGF is a damage signal that regulates neutrophil interstitial motility and inflammation through a HIF-1α pathway in response to tissue damage.

Introduction

Neutrophils are the first responders to tissue damage and are critical for mediating host defense to infection. However, excess neutrophil inflammation can also impair tissue repair. A key challenge is understanding how the migration and activation of neutrophils is controlled in sterile damage while maintaining critical host defense responses to microbial injury.

Acute tissue injury induces an array of signals that regulate neutrophil recruitment to damage in the absence of infection (de Oliveira et al., 2016). However, it is unclear how neutrophils differentially respond to tissue damage and microbial cues. Recent evidence suggests that tissue damage signals via phospholipase A2 are necessary for both sterile and microbial neutrophil recruitment (Huang and Niethammer, 2018). It remains unclear what distinguishes neutrophil responses to tissue damage signaling and microbial cues.

To address this question, we sought to identify factors that are present in sterile injury, but not infection (Houseright et al., 2020). We found that myeloid-derived growth factor (MYDGF) is up-regulated in leukocytes in response to wounding in zebrafish larvae. MYDGF has been reported to promote healing in a mouse model of myocardial infarction through effects on cell proliferation (Korf-Klingebiel et al., 2015; Wang et al., 2020). However, the role of MYDGF in regulating inflammation remains unclear.

Zebrafish larvae represent a powerful system to uncover new mechanisms that regulate inflammation due to their optical transparency, which enables noninvasive, real-time imaging of inflammation. Here, using real-time imaging, we show that MYDGF is a damage signal that influences neutrophil behavior in response to tissue damage signaling, but not microbial cues. The findings suggest that MYDGF functions as a newly identified inhibitor of neutrophils that promotes wound healing in larval zebrafish by providing a brake on neutrophil inflammation.

Results and discussion

mydgf expression is increased at wounds

We sought to identify factors that are increased by tissue damage, but not infection. Using translating ribosomal affinity purification gene expression analysis (Houseright et al., 2020), we found that *mydgf* is up-regulated in both neutrophils and macrophages in response to tail fin wounding (Fig. S1 A). In addition, *mydgf* expression was increased approximately fourfold in tail fins following two different types of tail fin injury, tail transection and thermal injury (Fig. S1 B). However, we detected no difference in *mydgf* expression in otic injection of *Pseudomonas aeruginosa* (Fig. S1 C), suggesting that *mydgf* expression is regulated by sterile injury, but not infection. These results, together with previous reports of increased *mydgf* expression in ischemia-reperfusion

[1]Department of Medical Microbiology and Immunology, University of Wisconsin-Madison, Madison, WI; [2]Department of Pediatrics, University of Wisconsin-Madison, Madison, WI; [3]Department of Biomolecular Chemistry, University of Wisconsin-Madison, Madison, WI.

*R.A. Houseright and V. Miskolci contributed equally to this paper; Correspondence to Anna Huttenlocher: huttenlocher@wisc.edu.

injury in mouse models (Korf-Klingebiel et al., 2015), suggest that up-regulation of *mydgf* is a common response to sterile tissue injury.

MYDGF regulates neutrophil responses to tissue damage, but not infection

MYDGF is highly conserved (53% amino acid identity and 79% similarity) between zebrafish and humans. Mapping the conserved residues onto the nuclear magnetic resonance (NMR) structure of human MYDGF (PDB accession no. 6O6W) reveals a near-complete conservation of the protein face opposite the N and C termini (Fig. 1 A). To characterize the role of MYDGF during wounding, we generated a zebrafish *mydgf* mutant using CRISPR-Cas9 gene editing, targeting exon 5 of *mydgf* and resulting in a 12-bp deletion (Fig. 1, B and C). *mydgf* homozygous mutants (*mydgf*$^{-/-}$) displayed loss of MYDGF protein by immunoblotting at 3 d postfertilization (dpf; Fig. 1 D). In agreement with previous reports in mice, we found that MYDGF-deficient zebrafish had no gross morphological defects and homozygous incrosses yielded normal larval growth (data not shown), suggesting that MYDGF is dispensable for normal development.

Next, we tested whether otic injury or administration of exogenous MYDGF altered neutrophil recruitment in WT and MYDGF-deficient larvae. Media from HEK293 cells transfected with zebrafish *mydgf* (*mydgf*-pCS2) showed secretion of MYDGF into the cell-conditioned media (CCM), as confirmed by immunoblotting (Fig. 1 E). Injection of control CCM showed increased neutrophil recruitment to the wound in the otic space in *mydgf*$^{-/-}$ larvae compared with control (Fig. 1, F and G), suggesting that endogenous MYDGF inhibits neutrophil infiltration. Injection of zebrafish MYDGF into the otic vesicle of WT larvae decreased neutrophil recruitment to the injury compared with larvae injected with control CCM, indicating that exogenous MYDGF is sufficient to inhibit neutrophil recruitment. Moreover, injection of MYDGF into the otic space of mutant larvae rescued the increased neutrophil accumulation (Fig. 1, F and G). Together, these findings show that depletion of MYDGF increases neutrophil recruitment to damaged tissues and that addition of exogenous MYDGF is sufficient to rescue the phenotype.

To determine if MYDGF regulates neutrophil recruitment to infection, we injected *P. aeruginosa* into the otic space, an established model of localized infection, and quantified neutrophil recruitment using Sudan Black staining (Deng et al., 2011). We found that depletion of MYDGF had no effect on neutrophil recruitment to *P. aeruginosa* (Fig. 1, H and I). Taken together, our findings suggest that MYDGF limits neutrophil recruitment to tissue damage, but not infection.

MYDGF-deficient larvae have a neutrophil-dependent defect in tail fin regeneration

Neutrophils impair wound healing in some contexts (Barros-Becker et al., 2020; Brubaker et al., 2013; Ebaid, 2014). Therefore, next we asked whether *mydgf*$^{-/-}$ larvae have altered tail fin regeneration in response to thermal injury, a model where the presence of neutrophils impairs wound healing (Barros-Becker et al., 2020). We found that MYDGF-deficient larvae had increased neutrophil recruitment to thermal injury at both 3 and 24 h postburn (hpb; Fig. 2, A and B), consistent with our findings with otic injury (Fig. 1 G). We also observed impaired wound healing of the tail fin following thermal injury at 24, 48, and 72 hpb (Fig. 2, C and D). This change is a specific defect in wound healing, as *mydgf*$^{-/-}$ larvae are developmentally similar to WT larvae and do not show a decrease in tail length in the absence of injury (Fig. S2 A). To determine if neutrophils mediate the impaired regeneration in MYDGF-deficient larvae, we depleted neutrophils from the wound using an established transgenic zebrafish expressing a dominant inhibitory Rac2 mutation (Rac2D57N) in neutrophils that renders neutrophils migration impaired (Deng et al., 2011). Control and Rac2D57N larvae were injected with either control morpholino oligonucleotides (mo) or mo targeting *mydgf*. Transient depletion of *mydgf* (Fig. S2 B) resulted in a 35–45% decrease in *mydgf* expression (Fig. S2, C and D) and increased neutrophil infiltration at wounds compared with control (Fig. S2, E–G), with no effect on total neutrophil numbers (Fig. S2 H). mo-mediated depletion of *mydgf* impaired regeneration in control larvae but had no effect on tail fin regeneration in the Rac2D57N larvae (Fig. 2, E and F). Together, these data show that depletion of MYDGF impairs regeneration and that this defect is due, at least in part, to the presence of neutrophils at the wound.

MYDGF-deficient larvae have altered neutrophil motility in the wound microenvironment

We imaged neutrophil recruitment in response to tissue damage to determine the effects of MYDGF on neutrophil behavior in the wound microenvironment. Neutrophil infiltration was also increased at tail transection wounds at 1 and 6 h post-wound (hpw) in MYDGF-deficient *Tg(mpx:mCherry)* larvae, with no change in total neutrophils (Fig. 3, A–C). To characterize the mechanism of persistent neutrophil inflammation, we imaged neutrophil behavior in the wound microenvironment and found that *mydgf*$^{-/-}$ larvae recruited more neutrophils to tissue damage, and these neutrophils remained in the wound microenvironment for a longer duration (Fig. 3, D and E). We analyzed the instantaneous speed of each neutrophil as they entered and left the wound microenvironment and found that after entering the wound, neutrophils slowed down in both WT and mutants; however, neutrophils in WT, but not mutants, increased their speed at later time points (Video 1). Within an hour of reaching the wound, neutrophils in WT larvae moved faster, with speeds approaching those at their entry into the wound, while neutrophils in *mydgf*$^{-/-}$ larvae maintained slow speeds (Fig. 3 F). These findings suggest that neutrophil behavior is different in MYDGF-deficient larvae, resulting in the retention of neutrophils in the wound microenvironment.

MYDGF-deficient larvae have impaired neutrophil reverse migration and resolution, without changes in macrophages

Neutrophil reverse migration is an important mechanism of inflammation resolution at sterile injury (Mathias et al., 2006; Wang et al., 2017). To determine whether the defect in inflammatory

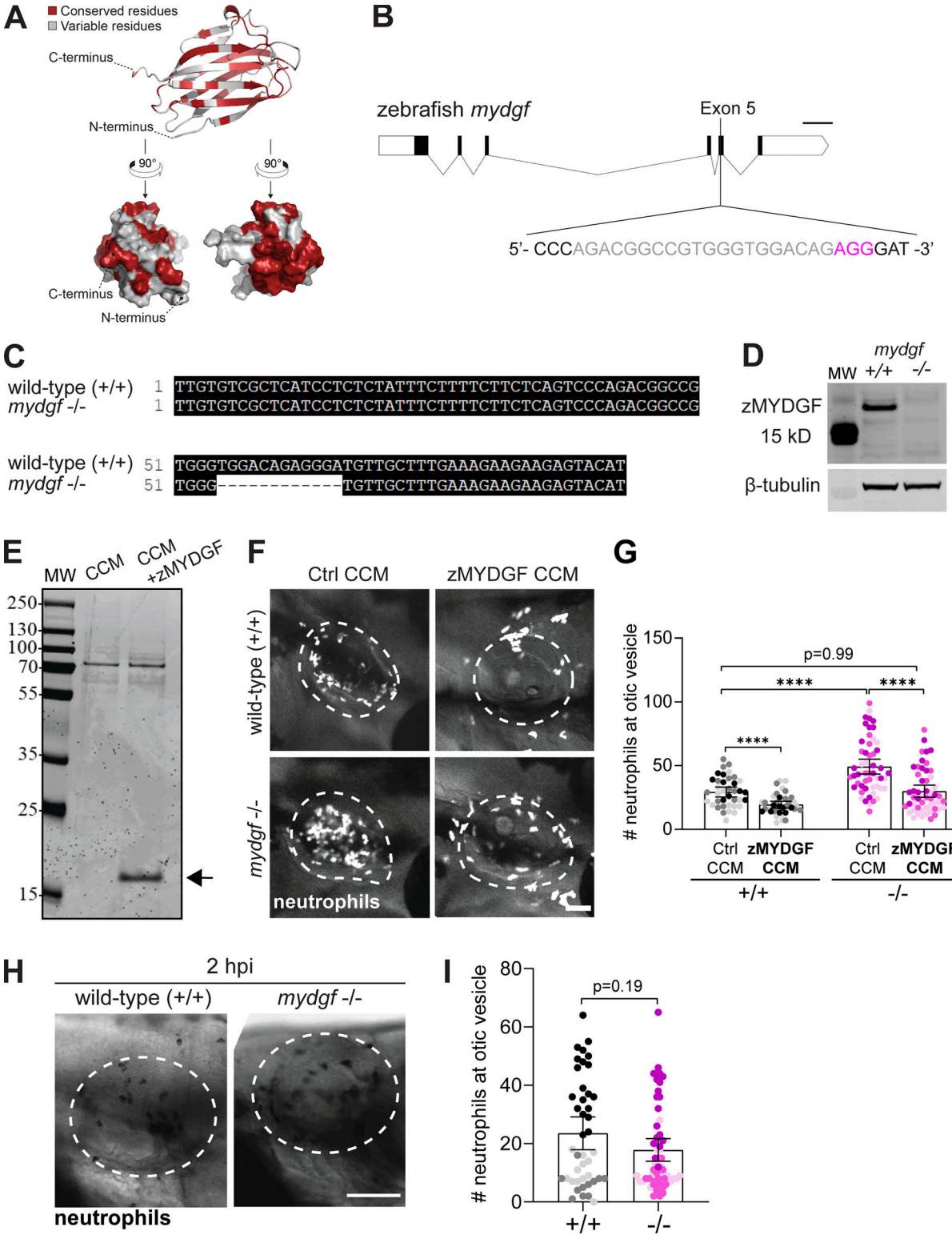

Figure 1. **MYDGF regulates neutrophil response to tissue damage, but not infection. (A)** Ribbon and surface representation of the human MYDGF NMR solution structure (PDB accession no. 6O6W). Residues identical in zebrafish MYDGF are shown in red. **(B)** Schematic of zebrafish *mydgf* gene, with exon 5 gRNA sequences highlighted for CRISPR-Cas9 mutagenesis. gRNA sequence is shown in gray and protospacer adjacent motif is shown in magenta; scale bar = 100 bp. **(C)** Exon 5 DNA sequence of WT (top) and *mydgf*$^{-/-}$ (bottom) zebrafish mutants showing a 12-bp deletion. **(D)** Representative Western blot for zebrafish MYDGF and β-tubulin from pooled 3 dpf zebrafish larvae. Data are representative of three independent replicates. Size marker (mol wt [MW]) in left lane. **(E)** InstantBlue stain of 12% SDS-PAGE of zebrafish MYDGF in CCM by HEK293 cells at 72 h after transfection by empty or zebrafish MYDGF-expressing pCS2 constructs. **(F and G)** Representative images (F) and quantification (G) of mCherry-labeled neutrophils at the otic vesicle of WT or *mydgf*$^{-/-}$ larvae, following microinjection with CCM ± zebrafish MYDGF protein at 2 h after injection; three independent replicates with *n* = 29 +/+ control, 32 +/+ zebrafish

MYDGF, 54 −/− control and 52 −/− zebrafish MYDGF; scale bar = 50 µm. **(H and I)** Otic vesicle of 3 dpf WT or *mydgf*$^{-/-}$ zebrafish larvae were microinjected with *P. aeruginosa (Pa;* 5000 CFU), followed by fixation at 2 h after injection. Neutrophils are visualized by Sudan Black staining. In H and I, representative brightfield images (H) and quantification (I) of the number of neutrophils at the otic vesicle are shown; three independent replicates with n = 43 +/+ and 57 −/−; scale bar = 100 µm. In G and I, data are expressed as mean with 95% CI; each symbol represents one larva, and different colors represent independent replicates. ****, P < 0.0001. P values were calculated by ANOVA with Tukey's multiple comparisons. Ctrl, control; hpi, h postinjection; zMYDGF, zebrafish MYDGF.

resolution in *mydgf*$^{-/-}$ larvae was due to impaired neutrophil reverse migration, we used the dendra2 photoconversion system to track neutrophil fate (Yoo and Huttenlocher, 2011). Neutrophils at the wound were photoconverted at 2 hpw, and the photoconverted neutrophils at the wound were quantified at 6 hpw (Fig. 4, A and B). We found that *mydgf*$^{-/-}$ larvae had increased numbers of both newly arrived neutrophils and lingering photoconverted neutrophils at the wound compared with WT larvae (Fig. 4, A and B). Furthermore, *mydgf*$^{-/-}$ larvae had significantly decreased resolution of neutrophils from the wound compared with WT larvae (Fig. 4 C). This defect in inflammatory resolution is also evident following the more robust thermal injury, with decreased resolution of neutrophils from the burn wound at 24 hpb (Fig. 4, D–F). Importantly, we did not observe a change in neutrophil apoptosis at the wound using caspase-3 staining (Fig. 4, G–I). Although macrophages mediate regeneration (Fig. S3, A and B), we did not observe altered macrophage recruitment or neutrophil-macrophage interactions (Tauzin et al., 2014) at wounds in *mydgf* mutants (Fig. S3, C–F; and Videos 1 and 2). Together, these data suggest that the accumulation of neutrophils in the wound in the MYDGF-deficient larvae is due to both increased recruitment of neutrophils and impaired neutrophil reverse migration.

Neutrophils accumulate in MYDGF-deficient larvae via HIF-1α pathway–dependent mechanisms

The HIF-1α pathway is an established regulator of neutrophil accumulation and resolution by reverse migration (Elks et al., 2011). Previous studies have shown that HIF-1α regulates resolution of inflammation by neutrophil reverse migration and apoptosis (Fig. 5 A). Given that this well-defined pathway produces a neutrophil recruitment phenotype similar to the one we observed in *mydgf*$^{-/-}$ larvae (Elks et al., 2011), we asked whether MYDGF exerts its function by modulating the HIF-1α pathway. We measured prolyl hydroxylase 3 (*phd3*) transcription using reverse transcription quantitative PCR (RT-qPCR) as a surrogate measure of HIF-1α activity (Walmsley et al., 2011). While expression did not differ between unwounded WT and *mydgf*$^{-/-}$ larvae, we detected a significant increase in *phd3* mRNA expression in *mydgf*$^{-/-}$ larvae following wounding (Fig. 5 B).

Next, we tested whether disrupting the HIF-1α pathway would reduce neutrophil accumulation in wounded *mydgf*$^{-/-}$ larvae using an established mo targeting *arnt-1*, a critical binding partner of HIF-1α (Fig. 5 A; Elks et al., 2011). We found that depletion of *arnt-1* in *mydgf*$^{-/-}$ larvae significantly decreased neutrophil numbers at the wound at both 1 and 6 hpw, similar to those observed in WT larvae (Fig. 5, C and D). These findings suggest that in the absence of MYDGF, HIF-1α activity is increased in response to tissue damage and leads to neutrophil accumulation at sites of tissue injury in a HIF-1α–dependent manner.

Our findings suggest that MYDGF functions as an endogenous inhibitor of neutrophil inflammation. Given its widespread expression (Bortnov et al., 2018), MYDGF may have a similar role in the regulation of inflammation in other tissues. Indeed, MYDGF expression is increased in a number of disease contexts in which the innate immune system is a major player, including diabetic nephropathy (He et al., 2020), rheumatoid arthritis (Weiler et al., 2007), and hepatocellular carcinoma (Sunagozaka et al., 2011).

The mechanisms by which MYDGF is secreted and exerts its effects are incompletely understood. MYDGF is a resident protein in the ER, and in silico modeling suggests docking of MYDGF with KDEL receptors (Bortnov et al., 2019). One of the consequences of ER stress is the release of resident ER proteins, including MYDGF (Trychta et al., 2018). Thus, MYDGF may be broadly released by stressed cells after tissue damage, and provide a beneficial effect by limiting neutrophil inflammation. Persistent neutrophil inflammation in tissues in *mydgf* mutants was dependent on the HIF-1α pathway, suggesting that MYDGF works with HIF-1α signaling to affect neutrophil accumulation in response to tissue damage.

In summary, we identified a new biological function for the paracrine factor MYDGF. We found that MYDGF is induced by sterile injuries and limits neutrophil inflammation in response to tissue damage, but not microbial cues. These findings provide new insight into an endogenous damage signal that puts the brakes on inflammation and neutrophil-mediated tissue injury.

Materials and methods

Zebrafish maintenance and handling

Animal care and use was approved by the Institutional Animal Care and Use Committee of University of Wisconsin and strictly followed guidelines set by the federal Health Research Extension Act and the Public Health Service Policy on the Humane Care and Use of Laboratory Animal, administered by the National Institutes of Health Office of Laboratory Animal Welfare. All protocols using zebrafish in this study were approved by the University of Wisconsin-Madison Research Animals Resource Center (protocol M005405-A02). AB and NHGRI-1 WT lines (LaFave et al., 2014) were used, as well as the previously published transgenic lines *mpx:mCherry* (Yoo et al., 2010) *mpeg1:GFP* (Ellett et al., 2011), *mpx:dendra2* (Yoo and Huttenlocher, 2011), *mpx:mCherry-2A-rac2* (Rosowski et al., 2016), and *mpx:mCherry-2A-rac2D57N* (Rosowski et al., 2016). Adult fish were maintained on a 14-h/10-h light/dark schedule. Following breeding, fertilized embryos were transferred to E3 medium (5 mM NaCl, 0.17 mM KCl, 0.44 mM $CaCl_2$, 0.33 mM $MgSO_4$, 0.025 mM

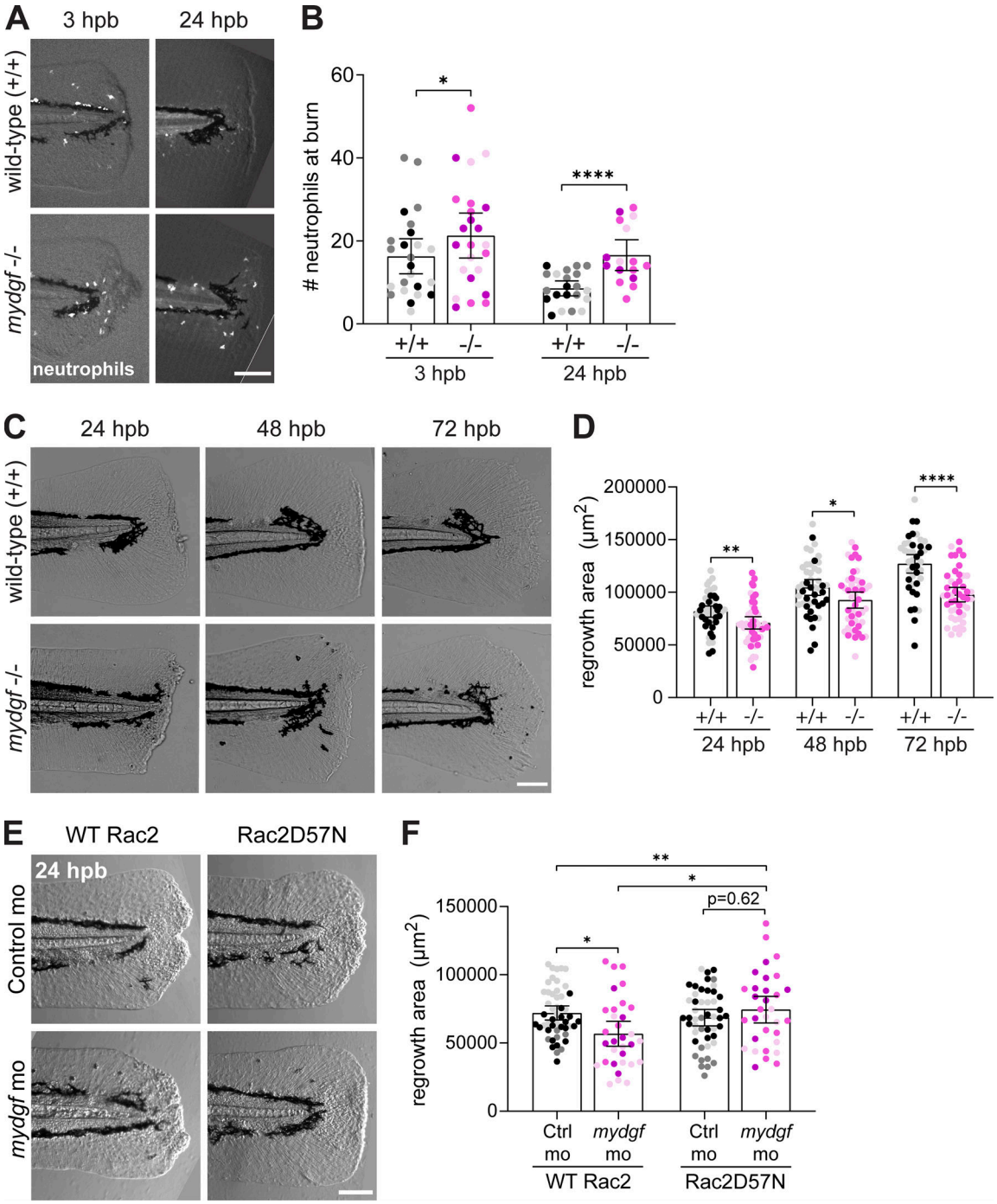

Figure 2. **MYDGF depletion leads to a neutrophil-dependent defect in wound healing. (A)** Caudal fins of 3 dpf WT or *mydgf*$^{-/-}$ zebrafish larvae with mCherry-labeled neutrophils were wounded by thermal injury and fixed at 3 and 24 hpb. Neutrophils were counted in the burn area. **(A and B)** Representative images (A) and quantification (B) of neutrophils in the burn are shown; three independent replicates with *n* = 24 +/+ and 24 −/− at 3 hpb and 21 +/+ and 16 −/− at 24 hpb; scale bar = 100 µm. **(C–F)** Caudal fins of 2 dpf (for morpholinos) or 3 dpf (for all other experiments) larvae were wounded by thermal injury and fixed at 24, 48, and 72 hpb. Wound healing was determined by quantifying the area of tail fin regrowth, measured from the caudal arteriovenous loop to the wound edge. **(C and D)** Representative brightfield images (C) and quantification (D) of tail fin regrowth area in WT and *mydgf*$^{-/-}$ larvae are shown; two independent replicates with *n* = 45 +/+ and 51 −/− at 24 hpb, 46 +/+ and 48 −/− at 48 hpb, and 41 +/+ and 47 −/− at 72 hpb; scale bar = 100 µm. **(E and F)** Representative brightfield images (E) and quantification (F) of tail fin regrowth area in WT (WT Rac2) or neutrophil motility–impaired (Rac2D57N) larvae, with or without *mydgf*-targeting morpholino #1, at 24 hpb; three independent replicates with *n* = 50 WT/control mo, 32 WT/*mydgf* mo, 48 D57N/control mo, and 32 D57N/*mydgf* mo; scale bar = 100 µm. In B, D, and F, data are expressed as mean with 95% CI; each symbol represents one larva, and different colors represent independent replicates. *, P < 0.05; **, P < 0.01; ****, P < 0.0001. P values were calculated by ANOVA with Tukey's multiple comparisons.

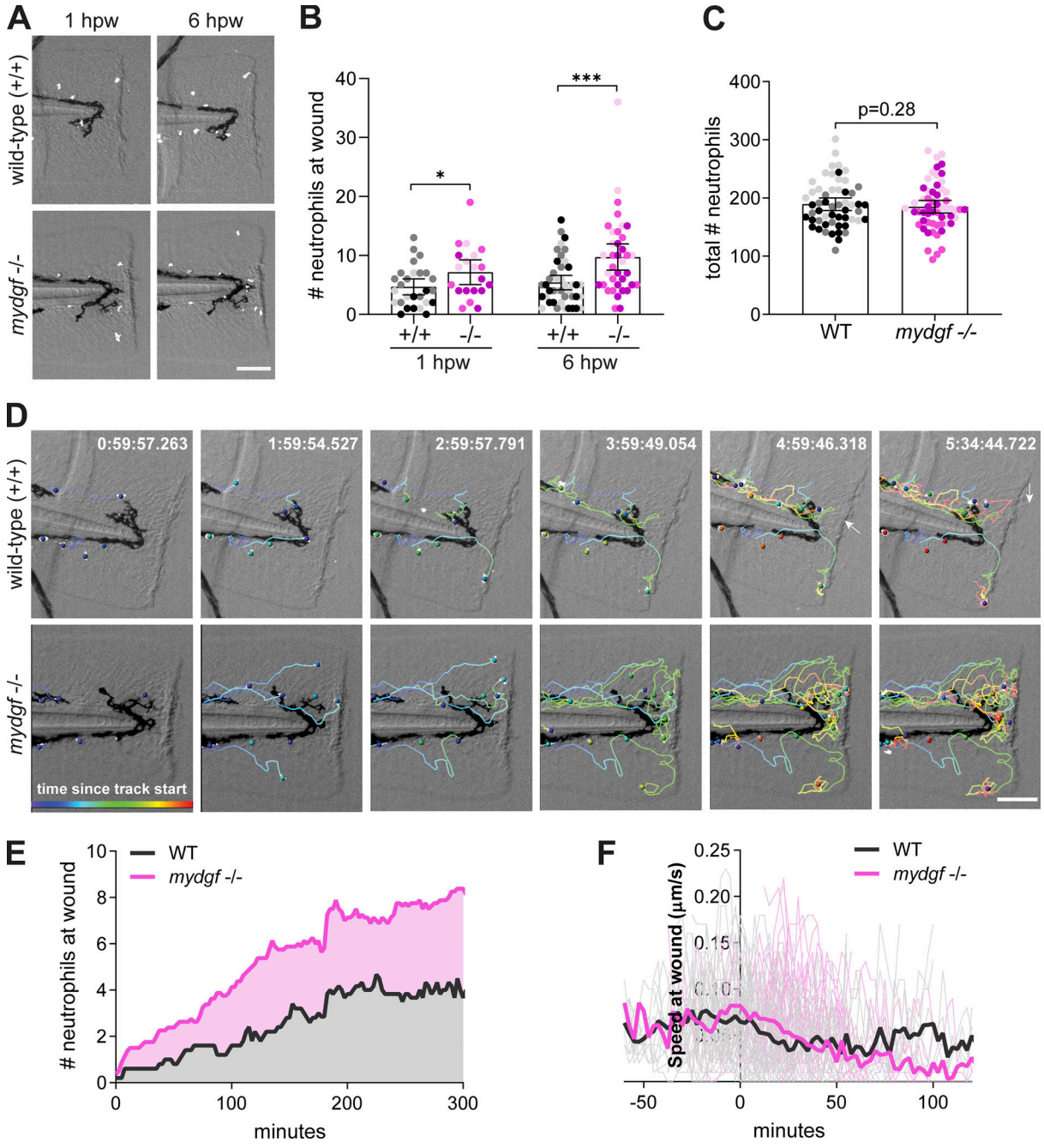

Figure 3. **MYDGF depletion alters neutrophil motility in the wound microenvironment. (A)** Caudal fins of 3 dpf WT or *mydgf*$^{-/-}$ zebrafish larvae with mCherry-labeled neutrophils were wounded by tail transection, and fixed at 1 and 6 hpw. Neutrophils were counted at the wound, distal to the tip of the notochord. **(A and B)** Representative images (A) and quantification (B) of neutrophils in the wound are shown; three independent replicates with n = 27 +/+ and 20 −/− at 1 hpw and 42 +/+ and 37 −/− at 6 hpw; scale bar = 100 µm. **(C)** Quantification of total number of mCherry-labeled neutrophils in 3 dpf WT and *mydgf*$^{-/-}$ whole larvae; three independent replicates with n = 55 WT and 58 −/−. In B and C, data are expressed as mean with 95% CI; each symbol represents one larva, and different colors represent independent replicates. *, P < 0.05; ***, P < 0.001. P values were calculated by ANOVA with Tukey's multiple comparisons. **(D)** Representative serial images from time-lapse imaging 0–6 h following tail transection of the caudal fin of WT and *mydgf*$^{-/-}$ larvae; see Video 1. Lines represent neutrophil tracks over time, with warmer colors indicating a longer time since track start; four independent replicates with n = 7 +/+ and 11 −/− larvae; scale bar = 100 µm. **(E)** Quantification of the number of neutrophils at the wound microenvironment over the course of time-lapse imaging. **(F)** Quantification of the instantaneous speed during the later phase (3–6 hpw) of neutrophil recruitment; 0 min represents the time at which each neutrophil enters the wound microenvironment.

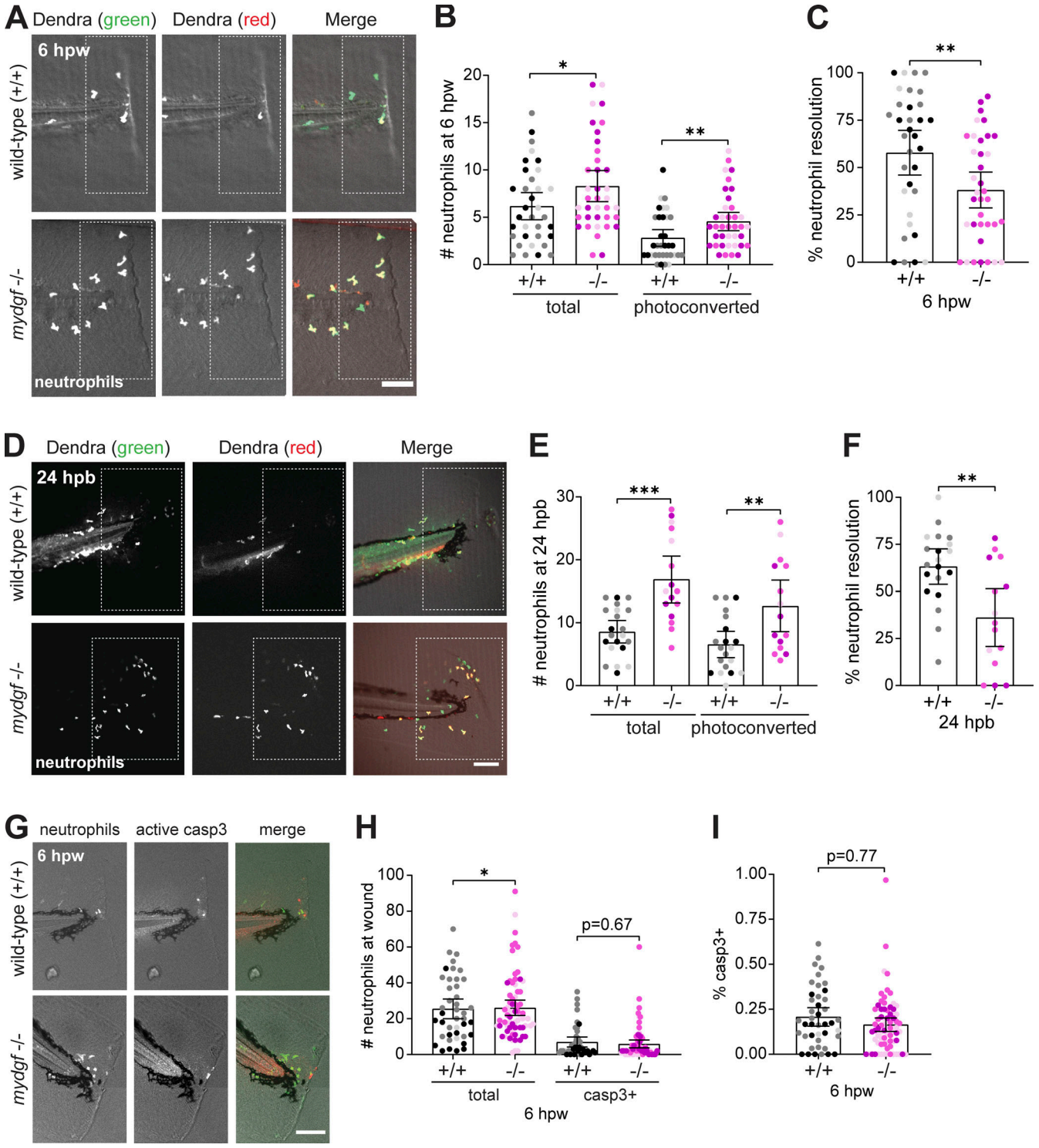

Figure 4. **MYDGF depletion impairs neutrophil reverse migration and resolution following injury. (A and B)** Representative images (A) and quantification (B) of green (total) and red (photoconverted) dendra2-labeled neutrophils in the wound microenvironment at 6 hpw following tail transection of 3 dpf WT and *mydgf*$^{-/-}$ larvae; three independent replicates with n = 33 +/+ and 36 −/−; scale bar = 100 µm. **(C)** Quantification of the percentage of photoconverted neutrophils present at the wound at 2 hpw that are no longer present at 6 hpw in the same larva. **(D and E)** Representative images (D) and quantification (E) of green (total) and red (photoconverted) dendra2-labeled neutrophils in the burn at 24 hpb following thermal injury of the caudal fin of 3 dpf WT and *mydgf*$^{-/-}$ larvae; three independent replicates with n = 20 +/+ and 15 −/−; scale bar = 100 µm. **(F)** Quantification of the percentage of photoconverted neutrophils present in the burn microenvironment at 3 hpb that are no longer present at 24 hpb in the same larva. **(G)** Representative images of immunostaining for active caspase-3 (casp3) following tail transection of 3 dpf WT and *mydgf*$^{-/-}$ larvae with mCherry-labeled neutrophils at 6 hpw; scale bar = 100 µm. **(H)** Quantification of total and active caspase-3–expressing neutrophils in the wound at 6 hpw; three independent replicates with n = 42 +/+ and 71 −/−. **(I)** Proportion of neutrophils in the wound expressing active caspase-3 at 6 hpw. In B, C, E, F, H, and I, data are expressed as mean with 95% CI; each symbol represents one larva, and different colors represent the results of three independent replicates. *, P < 0.05; **, P < 0.01; ***, P < 0.001. P values were calculated by ANOVA with Tukey's multiple comparisons.

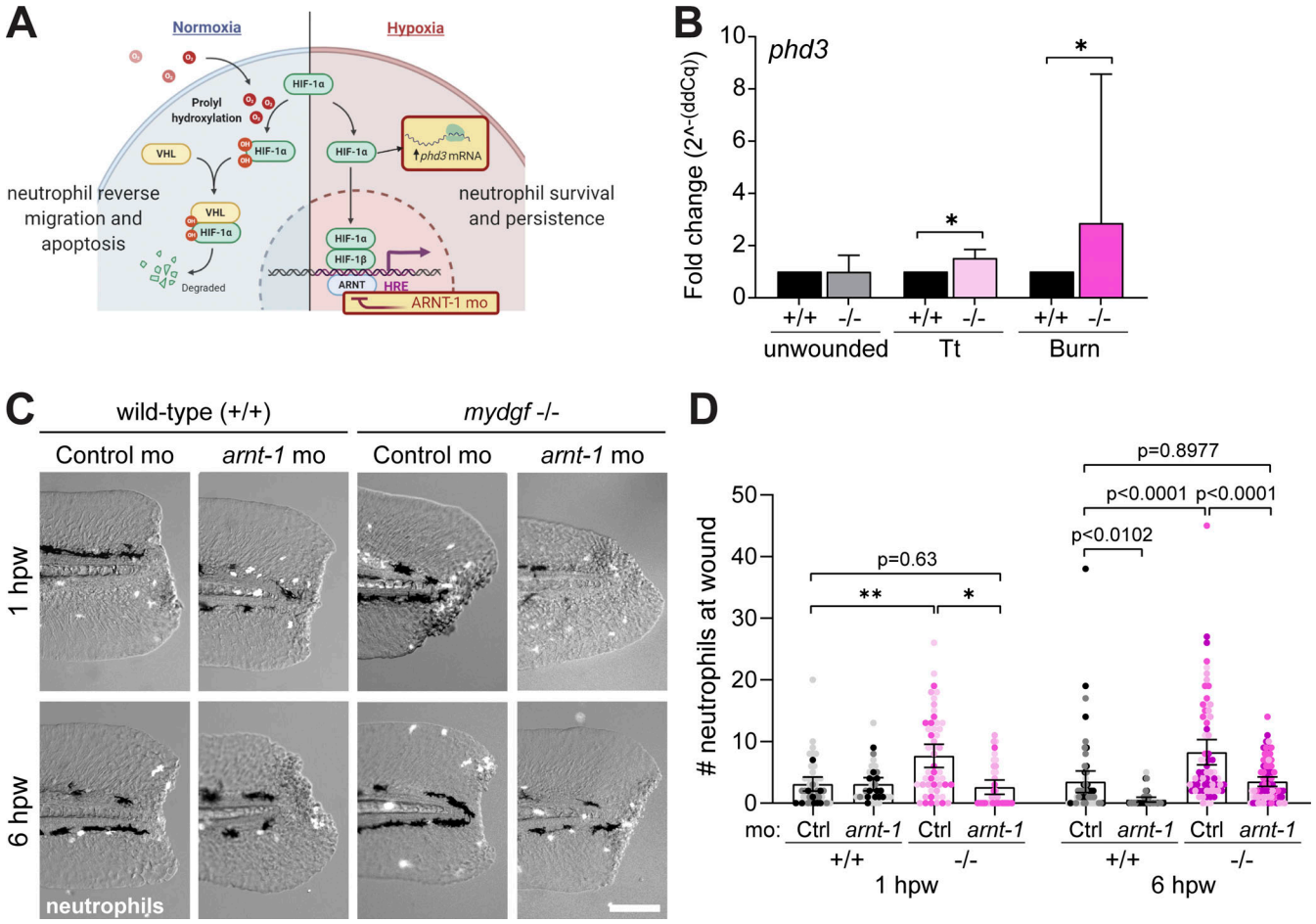

Figure 5. **Neutrophil accumulation in the *mydgf* mutant is dependent on the HIF-1α pathway. (A)** Schematic representation of HIF-1α activation in neutrophils. Pathway activation results in neutrophil persistence and survival and is characterized by increased expression of *phd3*. HIF-1α pathway activation can be blocked at the level of transcription factor nuclear binding using arnt-1 morpholino. Illustration was created at www.biorender.com. **(B)** *phd3* expression in pooled tail fin tissue collect from WT larvae, either unwounded or 3 h following tail transection (Tt) or thermal injury (burn), measured by RT-qPCR. Data comprise three (burn) to five (Tt) independent replicates performed in technical triplicates and normalized to *mydgf* expression in unwounded tails and to *ef1α*. n = 50 tails per condition per independent replicate. *, P < 0.05. Fold changes in gene expression were compared with the normalized value of 1 using one-sample t tests. **(C and D)** Representative images (C) and quantification (D) of the number of mCherry-labeled neutrophils at the wound in WT and *mydgf*$^{-/-}$ larvae, with control or *arnt-1* morpholino, at 1 and 6 hpw after Tt; three or four independent replicates with n = 46 +/+ control mo, 33 +/+ *arnt-1* mo, 50 −/− control mo, and 38 −/− *arnt-1* mo at 1 hpw and 54 +/+ control mo, 38 +/+ *arnt-1* mo, 68 −/− control mo, and 73 −/− *arnt-1* mo at 6 hpw; scale bar = 100 µm. Data are expressed as mean with 95% CI; each symbol represents one larva, and different colors represent independent replicates. *, P < 0.05; **, P < 0.01. P values were calculated by ANOVA with Tukey's multiple comparisons.

NaOH, and 0.0003% Methylene Blue) and maintained at 28.5°C. Larval zebrafish were anesthetized using 0.2 mg/ml tricaine (ethyl 3-aminobenzoate; Sigma-Aldrich) before any experimentation or live imaging.

RT-qPCR

Tail tissue distal to the caudal yolk extension was dissected from 3 dpf larvae following a 15-min incubation over ice. Approximately 50 tails per condition were pooled, and RNA was extracted using TRIZOL reagent (Invitrogen), according to the manufacturer's instructions. cDNA was synthesized from the RNA using the SuperScript III FirstStrand Synthesis System with Oligo(dT) (Thermo Fisher Scientific). qPCR was performed using FastStart Essential Green Master (Roche) and a LightCycler 96 (Roche). Data were normalized to *ef1α* using the ΔΔCq method (Livak and Schmittgen, 2001) and expressed as fold change ($2^{-\Delta\Delta Cq}$) over pooled WT or unwounded larvae. The following primers were used: *mydgf* (forward, 5′-CCCAAGGGAAGTCCTACTTG-3′; reverse, 5′-AGCAACATCCCTCTGTCCAC-3′), *phd3* (forward, 5′-CGCTGCGTCACCTGTATT-3′; reverse, 5′-TAGCATACGACGGCTGAACT-3′), and *ef1α* (forward, 5′-TGCCTTCGTCCCAATTTCAG-3′; reverse, 5′-TACCCTCCTTGCGCTCAATC-3′). All PCR reactions were performed in triplicate.

Multiple sequence alignment between human and zebrafish MYDGF

A MUSCLE alignment was generated in Jalview using the protein sequences of mature human MYDGF (UniProtKB accession no. Q969H8; residues V32-L173), mature zebrafish MYDGF (UniProtKB accession no. Q6DGL1; E27-L164; The UniProt Consortium, 2017), and the 22 seed sequences of MYDGF homologues provided in Pfam (Pfam accession no. PF10572).

The 80 residues of human MYDGF that were identical to zebrafish MYDGF in the sequence alignment (58% sequence identity) were mapped onto the NMR solution structure of human MYDGF. The structure presented herein was solved using NMR data (Bortnov et al., 2019) to obtain a refined solution structure of human MYDGF that has been subsequently reconciled with the crystal structure (Ebenhoch et al., 2019) as described in (Bortnov, 2020) and deposited under PDB accession no. 6O6W.

Morpholino injections

Splice-blocking morpholinos were designed to the exon 3/intron 3 border and exon 5/intron 5 border of *mydgf*. Morpholinos were obtained from GeneTools and resuspended in water to a stock concentration of 1 mM. Morpholinos were further diluted to a final concentration of 350 µM, and 3 nl of this injection mix was injected into the yolk sac of zebrafish embryos at the one-cell stage. Morpholino sequences are as follows: *mydgf E3I3* (#1), 5′-GAGTGTATAAGTTACCTCCATACTG-3′; mydgf E5I5 (#2), 5′-GGAATAGCATATACGCATGCTCACC-3′; mismatch control, 5′-CCTCTTACCTCAGTTACAATTTATA-3′. A previously published morpholino targeting *arnt-1*, 5′-GGATTAGCTGATGTC ATGTCCGACA-3′ (Prasch et al., 2006), was obtained from GeneTools and resuspended in water to a stock concentration of 1 mM. Morpholinos were further diluted to a final concentration of 500 µM and injected as above.

Generation of a zebrafish *mydgf* mutant and genotyping

Short guide RNA targeting zebrafish *mydgf* (ENSDARG00000071679) was designed using CHOPCHOP (Montague et al., 2014). The exon 5 target sequence was 5′-GGCCGTGGGTGGACAGG-3′. CRISPR-Cas9 gRNA synthesis and injections were performed as previously described (Gagnon et al., 2014). NHGRI-1 embryos were injected in the yolk sac at the one-cell stage with 150 pg short guide RNA and 300 pg Cas9 protein (#CP01-50; PNA Bio). To confirm genome editing, genomic DNA was extracted from 2 dpf larvae and amplified using the following primers: forward, 5′-GTAAAACGA CGGCCAGTGTGACATTGACATTTGCCGCA-3′; reverse, 5′-AGACTC TGACACTATGTACTCT-3′. The PCR fragments were separated on a 3% agarose gel.

Sequences of F0 mosaic cuts were confirmed by topoisomerase-based cloning (Zero Blunt TOPO PCR Cloning Kit; Thermo Fisher Scientific) and sequencing. Clutches of larvae with confirmed CRISPR cuts were grown to adulthood. Adult F0 CRISPR-injected fish were screened for germline mutations by DNA extraction and topoisomerase-based cloning and sequencing of sperm or eggs from individual fish.

Heterozygous *mydgf* mutants were obtained by outcrossing the CRISPR mutants to AB WT zebrafish. Offspring were genotyped using genomic DNA obtained from fin clips and amplified using the primers listed above. The PCR product was separated on a 3% agarose gel to determine individual fish genotypes. F2 and/or F3 heterozygotes were in-crossed to generate homozygous $mydgf^{+/+}$ (WT) and $mydgf^{-/-}$ siblings. For experimental purposes, these fish were grown to adulthood and in-crossed to produce clutches of WT and $mydgf^{-/-}$ cousins. These cousins were used only for experiments and not for line maintenance or the production of future generations.

Expression and purification of zebrafish MYDGF

The insert encoding mature zebrafish MYDGF (UniProtKB accession no. Q6DGL1; E27-L164) was amplified by PCR from cloned *Danio rerio* using primers (5′-CTGTGTGGTACCGAAAGG ACCAAAACACTGGACTTCG; 3′-TAGAGGGCTAGCTCAGAGTTC ATCATGCCGTATTCGAC), which introduced restriction sites for cloning (5′ Kpn1 and 3′ Nhe1) into pET.ELMER (Maurer et al., 2010). Sequences were verified before expression in bacteria.

BL21 (DE3) competent cells (#69450; MilliporeSigma) were transformed with the pET.ELMER-zebrafish MYDGF plasmid and protein expression was induced using 1 mM isopropyl β-D-1-thiogalactopyranoside (IPTG) as previously described (Bortnov et al., 2019). The recombinant protein was expressed with an N-terminal polyhistidine tag and thrombin cleavage site (residues MGGSHHHHHHGSLVPRGSKGT) preceding the mature zebrafish MYDGF sequence. The recombinant protein was extracted in an 8 M urea cell lysis solution and purified by immobilized metal affinity chromatography using nickel-nitrilotriacetic acid resin (#30230; Qiagen) as detailed previously (Bortnov et al., 2019). The protein was then refolded through dialysis against dilute acetic acid (100 mM, then 1 mM; pH 3.7), which removed components of the cell lysis solution and maximized protein solubility. After screening a variety of buffers and pH conditions, we determined that this protein construct was especially insoluble in buffers containing NaCl concentrations above 100 mM and in pH environments above pH 6. The protein was ultimately dialyzed against a pH 6.0 buffer solution containing 10 mM sodium phosphate, 100 mM NaCl, and 0.5 mM dithiothreitol and purified by size-exclusion chromatography on a HiLoad 16/600 Superdex 75 prep grade column (#28-9893-33; Sigma-Aldrich) equilibrated in and eluted with the same buffer. After verification by SDS-PAGE, fractions containing only monomeric zebrafish MYDGF were combined, and the final sample was concentrated using an Amicon Ultra-4 centrifugal filter (#UFC801024; MilliporeSigma).

Antibody production and Western blotting

The zebrafish MYDGF immunogen described above was submitted to Covance Research Products Immunology Services for generation of rabbit anti-zebrafish MYDGF antiserum. Antiserum was exposed to Protein A Sepharose beads overnight at 4°C to absorb total IgG and then washed in 50 times the bead volume PBS plus 0.1% tween and 0.5% NP-40, and in two times the bead volume PBS only. IgG was eluted with 2 × 500 µl 100 mM glycine, pH 3.0, and neutralized with 1/10th volume 1 M Tris, pH 8.0. OD at 280 nm was taken for IgG concentration.

For Western blotting, 50–100 2 dpf larvae were pooled and deyolked in calcium-free Ringer's solution with gentle disruption from a p200 pipette tip. Larvae were washed twice with PBS and stored at −80°C until samples were lysed by sonication in 20 mM Tris, pH 7.6, 0.1% Triton X-100, 0.2 mM PMSF, 1 µg/ml Pepstatin, 2 µg/ml Aprotinin, and 1 µg/ml Leupeptin at 3 µl per larvae while on ice and clarified by centrifugation. Protein concentrations were determined using a bicinchoninic acid protein assay kit (Thermo Fisher Scientific), according to the manufacturer's instructions. Equal amounts of total protein were loaded on 12% SDS-polyacrylamide gels and transferred to

nitrocellulose membrane. Affinity-purified total rabbit anti-zebrafish MYDGF was used at 1:500 dilution. Actin (monoclonal actin AC15; #A5441; Sigma-Aldrich) or β-tubulin (mouse β-tubulin [D3U1W]; #86298; Cell Signaling Technology) was detected for loading control. Western blots were imaged and quantified by normalizing to loading controls with an Odyssey Infrared Imaging System (LI-COR Biosciences). The antibody did not work for immunofluorescence.

MYDGF protein production and injection

HEK293 cells were transfected with zebrafish *mydgf*-pCS2 or empty pCS2 constructs using Lipofectamine 3000 reagent (#L3000008; Invitrogen) following the manufacturer's protocol. 16–20 h after transfection, cell media was changed to SFM4HEK293 media (HyClone; Thermo Fisher Scientific). 72 h later, media was collected, clarified by centrifugation, and aliquoted and frozen at −80°C. Samples of media were run on 12% SDS-polyacrylamide gels and checked by Western blot and InstantBlue staining (Abcam).

CCM with and without zebrafish MYDGF were mixed at two parts media to one part phenol red. Tricaine-anesthetized 3 dpf WT or *mydgf*$^{-/-}$ *mpx:mCherry* zebrafish larvae were injected with 1 nl of the injection mix in the left otic vesicle. At 2 h after injection, larvae were fixed in 4% PFA at 4°C, and the area of the otic vesicle was imaged as described below.

Tail transection of the caudal tail fin

Dechorionated, tricaine-anesthetized 3 dpf larvae were transferred to milk-coated 35-mm plates, washed twice in E3 medium, and wounded in 0.2 mg/ml tricaine/E3 solution. Tail transection was performed using a #10 scalpel blade just distal to the tip of the notochord. Larvae were transferred to zebrafish Wounding and Entrapment Device for Growth and Imaging (ZWEDGI) devices (Huemer et al., 2017), or washed 3 times in E3 medium and allowed to recover at 28.5°C until live imaging or fixation at indicated times.

Thermal injury of the caudal tail fin

Thermal injury to the caudal fin was performed as previously described (Miskolci et al., 2019). Briefly, a fine tip (type E) of a line-powered thermal cautery instrument (Stoelting) was applied to the distal tip of the tail fin of tricaine-anesthetized larvae in the E3 medium for 1–2 s until the tail fin tissue curled but before injury to the notochord was observed. Following injury, the larvae were transferred to ZWEDGI devices or washed with E3 medium and allowed to recover at 28.5°C until live imaging or fixation at indicated times.

Otic vesicle injection

5,000 colony-forming units (CFUs) of *P. aeruginosa* were microinjected in 1 nl volume as previously described (Harvie and Huttenlocher, 2015). Bacterial suspension (10,000 CFU/nl) was further diluted 1:1 with PBS containing 10% glycerol, 2% PVP-40 (polyvinylpyrrolidine; Sigma-Aldrich), and 0.33% phenol red, to a final concentration of 5,000 CFU/nl. PVP-40 was used to prevent bacterial clumping and phenol red was used to visualize injection success. Tricaine-anesthetized larvae positioned laterally on an angled injection ramp made of 2% agarose in E3 medium (in 10-cm Petri dish) and pretreated with 1 ml filter-sterilized 2% BSA to prevent larval abrasions. 1 nl volume was microinjected into otic vesicle using a thin-walled glass capillary injection needle, with time range set to "millisecond" and pressure set to ∼20 PSI on the microinjector. 2 h after injection, larvae were fixed in 4% PFA at 4°C. Larvae were stained by Sudan Black to visualize neutrophils.

Preparation of bacteria

GFP-expressing *P. aeruginosa* (pMF230) was prepared for microinjection as previously described (Rosowski et al., 2016). A single colony was grown overnight in Miller LB medium (#DSL24400; Dot Scientific) without antibiotics at 37°C with shaking. In the morning, the culture was diluted 1:5 and grown for an additional 1 h 15 min at 37°C with shaking. OD at 600 nm was measured to calculate CFUs/nl (OD 1 = ∼2.6 × 10^5 CFUs/ml). Bacterial suspension was pelleted by centrifugation for 30 s at ∼21,000 ×*g*, washed three times, and resuspended in sterile PBS at 10,000 CFUs/nl.

Sudan Black staining

Larvae were fixed in 4% PFA at 4°C until staining. Larvae were washed three times in PBS and then incubated for 30 min in Sudan Black B working solution (0.18% stock diluted 1:5 in 70% ethanol; 0.1% phenol). Larvae were washed twice in 70% ethanol. Depigmentation was performed by incubating the larvae in a solution of 1% potassium hydroxide and 1% H_2O_2 for 10 min. The larvae were washed and then stored at 4°C in a solution of 0.1% Tween-20 in PBS.

Neutrophil recruitment assays

2 dpf morpholino-injected WT AB and *mpx:mCherry* or 3 dpf WT and *mydgf*$^{-/-}$ *mpx:mCherry* zebrafish larvae were wounded by tail transection or thermal injury, or injected with zebrafish MYDGF protein in the otic vesicle, as described above. Larvae were fixed in 4% PFA at 4°C at 1 and 6 hpw (following tail transection), 3 and 24 hpb (following burn wound) or 2 h after otic vesicle injection. Caudal fins were imaged in PBS at room temperature on a Zeiss Zoomscope (EMS3/SyCoP3; 1× Plan-NeoFluar Z objective; Zeiss) with an Axiocam Mrm charge-coupled device camera using ZenPro 2012 software (Zeiss). For protein injection assays, images of the otic vesicle region were acquired in PBS at room temperature on a spinning-disk confocal (CSU-X; Yokogawa) on a Zeiss Observer Z.1 inverted microscope and an electron-multiplying charge-coupled device Evolve 512 camera (Photometrics), with a Plan-Apochromat 20×/NA 0.8 air objective (5-µm optical sections, 2,355 × 512 resolution) using ZenPro 2012 software (Zeiss). Neutrophil numbers were counted manually in z-projected images using Zen 2.3 Lite software (Zeiss). Neutrophil numbers were counted in the area distal to the tip of the notochord (tail transections), the area distal to the caudal vessel loop (burn wounds), or within the confines of the otic vesicle (protein injections).

Total neutrophil counts

2 dpf morpholino-injected WT AB or 3 dpf WT and *mydgf*$^{-/-}$ *mpx:mCherry* unwounded zebrafish larvae were fixed in 1.5% formaldehyde (FA; Polysciences) in 0.1 M Pipes (Sigma-Aldrich), 1.0 mM $MgSO_4$ (Sigma-Aldrich), and 2 mM EGTA (1.5% FA solution; Sigma-Aldrich) overnight at 4°C. Images were acquired at room temperature using a spinning-disk confocal microscope as described above (20×/NA 0.8 air objective, 10-µm optical sections, 2 × 6 tiles, 2,355 × 512 resolution) using ZenPro 2012 software (Zeiss). Tiles were stitched together, and neutrophils were counted manually in z-projected images using Zen 2.3 Lite software (Zeiss).

Wound-healing assays

Tricaine-anesthetized 3 dpf WT and *mydgf*$^{-/-}$ larvae were wounded by tail transection or thermal injury, as described above. Larvae were washed three times with E3 medium and allowed to regenerate for 3 d after injury at 28.5°C. During regeneration, larvae were fixed in 4% PFA at 4°C at 24, 48, and 72 h after injury. Fins were imaged in PBS at room temperature using a Zeiss Zoomscope, as described above. Unwounded, age-matched larval fins were collected and imaged as a developmental control. Regenerate or developmental area of the tail fins was measured from the distal tip of the notochord (tail transection) or the caudal vessel loop (burns) using FIJI image analysis software (Rueden et al., 2017).

To quantify neutrophil contributions to burn regeneration with or without MYDGF, *mpx:mCherry-2A-rac2* or *mpx:mCherry-2A-rac2D57N* larvae (Rosowski et al., 2016) were injected with *mydgf*-targeting or mismatch control morpholinos as described above and incubated to 2 dpf at 28.5°C. The larvae were then wounded by thermal injury at the caudal fin, washed three times with E3 medium, allowed to regenerate for 24 hpb, and fixed in 4% PFA. Fins were imaged and measured as described above.

Live imaging and image analysis/processing

3 dpf WT and *mydgf*$^{-/-}$ *mpx:mCherry/mpeg1:GFP* larvae were wounded by tail transection or thermal injury, as described above. Larvae were mounted in ZWEDGI devices (in 0.2 mg/ml tricaine/E3 solution and held in place using 1% low-melting-point agarose, applied at the head) or embedded in 1% low-gelling agarose (Sigma-Aldrich) containing 0.2 mg/ml tricaine in an Ibidi µ-slide two-well glass bottom chamber (Ibidi). Images of the caudal fin region were acquired at room temperature using a spinning-disk confocal microscope (10×/NA 0.3 or 20×/NA 0.8 air objective, 5-µm optical sections, one z-stack every 2.5 min for 3 or 6 h at indicated times following injury). 3D cell tracking was performed using Imaris image analysis software (Bitplane). Leukocytes were tracked using the "Spots" function, where spot size was defined as a range of 12–15 µm. Individual tracks were curated after software detection. Tracks were then filtered according to the following criteria to eliminate false tracks and tracks showing only vibrational or nonprogressive movement; short tracks comprising fewer than five spots for neutrophils, tracks with a total displacement length of less than 14 µm (neutrophils), and tracks with a mean track speed of 0 µm/s were eliminated. For experiments comparing neutrophil instantaneous speed with position relative to the notochord, the x-position of each spot over the course of the track is normalized to the x-position of the tip of the notochord for the individual larva being measured. For experiments quantifying neutrophil-macrophage contact, the absolute number of neutrophils and macrophages for each frame was normalized using the formula # of contacts × number of neutrophils/number of macrophages.

Dendra2 photoconversion

3 dpf WT or *mydgf*$^{-/-}$ *mpx:dendra* larvae were wounded by tail transection or thermal injury, as described above. Tricaine-anesthetized larvae were mounted in ZWEDGI devices and held in place using 1% low melting point agarose, applied to the head. An imaging sequence was performed on each larva comprising an initial z-stack of the caudal fin area, followed by photoconversion of the neutrophils caudal to the tip of the notochord (tail transection) or vessel loop (burn wounds) and second z-stack of the caudal fin area after photoconversion. The photoconversion and associated imaging sequences were performed at room temperature using a laser-scanning confocal microscope (FluoView FV-1000, 20×/NA 0.75 air objective; Olympus). The following stimulation settings were used for photoconversion: 40% 405 nm laser transmissivity, 10 µs/pixel dwell time, and 45 s total stimulation time. Photoconversion was performed at 2 hpw for tail transections and 4 hpb for burn wounds. Larvae were maintained in E3 medium in individual wells of a 96-well plate at 28.5°C until final imaging.

At 6 hpw (tail transections) or 24 hpb (burn wounds), larvae were fixed in 1.5% FA solution overnight at 4°C. Larvae were then mounted in 1% low-melting-point agarose, and images of the tail region were acquired using a spinning-disk confocal microscope, as described above for neutrophil recruitment assays. Photoconverted (red) and nonphotoconverted (green) neutrophils in the area distal to the tip of the notochord (tail transections) or distal to the vessel loop (burn wounds) were counted manually using FIJI image analysis software (Rueden et al., 2017).

Quantification of apoptosis

Immunostaining to identify apoptotic (active caspase-3 positive) neutrophils was performed using 3 dpf WT or *mydgf*$^{-/-}$ *mpx:mCherry* larvae. Larvae wounded by tail transection were fixed at 6 hpw in 4% PFA at 4°C overnight and then stored in methanol at −20°C until immunostaining. Larvae were incubated with monoclonal rabbit anti-active caspase-3 antibody (#559565; BD Biosciences) at 1:200 in block (PBS, 1% DMSO, 1% BSA, 0.05% Triton X-100, and 1.5% goat serum), followed by incubation with Alexa Fluor 488 donkey anti-rabbit secondary antibody (Thermo Fisher Scientific). The caudal fin area was then imaged at room temperature in PBS using a spinning-disk confocal microscope, as described above (20×/NA 0.8 air objective, 5-µm optical sections). Apoptotic neutrophils were defined as discrete spots in the area distal to the tip of the notochord expressing both red (neutrophil) and green (active caspase-3) fluorescence. Apoptotic neutrophils were counted manually using Zen 2.3 Lite software (Zeiss).

Macrophage depletion

Macrophage depletion was performed by injection of clodronate liposomes. At 2 dpf, anesthetized (*Tg(mpeg1:GFP)*) larvae were injected intravenously via the posterior caudal vein with 1 nl liposome-encapsulated clodronate (www.clodronateliposomes.org) or PBS. The clodronate liposome–injected fish were sorted for GFP-negative (macrophage depleted) larvae. Thermal injury of the caudal fin was performed on GFP-negative larvae, along with PBS liposome–injected controls at 3 dpf. The wound healing of larvae was monitored over time by live imaging at room temperature in 0.2 mg/ml tricaine/E3 medium at 1, 2, 3, and 4 d after burn on a Zeiss Zoomscope (EMS3/SyCoP3; 1× Plan-NeoFluar Z objective; Zeiss) with an Axiocam Mrm charge-coupled device camera using ZenPro 2012 software (Zeiss). Tail fin regrowth area was then measured for each larva as described above.

Statistical analyses

Independent biological replicate is defined as a separate clutch of larvae spawned on different days. RT-qPCR gene expression analyses comprised three to five independent biological replicates, and reactions were performed in three technical replicates. Statistical significance was determined by comparing the calculated ΔCq of the experimental conditions using the nonparametric Wilcoxon two-group test. Fold change in ΔCq was calculated and plotted in terms of mean with 95% confidence interval (CI). Neutrophil quantification and migration analyses and regeneration assays comprised three or four biological replicates. Replicate numbers are noted in the figure legends. Experimental conditions were compared using analysis of variance. Comparisons between two groups were performed using an unpaired, two-tailed t test. Data distribution was assumed to be normal, but this was not formally tested. For quantification of neutrophil instantaneous speed over position, a linear mixed effect regression model was used. Genotype and position were treated as fixed effects, with experimental replicate, fish, and neutrophil (within fish) treated as random effects. Statistical analyses were performed in R version 3.5.1 (www.r-project.org) using the associated lme4 package. Reported P values are two sided, and the level of statistical significance was preset to 0.05, with no adjustment for multiplicity.

Online supplemental material

Fig. S1 displays *mydgf* expression in response to sterile wounds and infection as measured by translating ribosome affinity purification RNA sequencing and qPCR. Fig. S2 shows efficiency of morpholino-mediated depletion of *mydgf* and recruitment of neutrophils to tail transection and total number of neutrophils in morpholino-depleted zebrafish larvae. Fig. S3 depicts the characterization of macrophage response and neutrophil–macrophage interaction at sterile wounds. Video 1 shows neutrophil and macrophage response following tail transection of the caudal fin. Video 2 shows neutrophil and macrophage response following thermal injury of the caudal fin.

Acknowledgments

We thank members of the Huttenlocher laboratory for valuable discussions.

This work was supported by the National Institutes of Health (grant R35GM118027 to A. Huttenlocher and grant T32HL07899 to R.A. Houseright) and the American Heart Association (fellowship 17POST33410970 to V. Miskolci).

The authors declare no competing financial interests.

Author contributions: R.A. Houseright and A. Huttenlocher conceived and designed experiments. R.A. Houseright, V. Miskolci, O. Mulvaney, D.A. Bennin, and J. Rindy conducted the experiments and analysis. R.A. Houseright, V. Miskolci, D.F. Mosher, V. Bortnov, and A. Huttenlocher prepared the figures and wrote the manuscript.

Submitted: 9 March 2021
Revised: 25 April 2021
Accepted: 6 May 2021

References

Barros-Becker, F., J.M. Squirrell, R. Burke, J. Chini, J. Rindy, A. Karim, K.W. Eliceiri, A. Gibson, and A. Huttenlocher. 2020. Distinct Tissue Damage and Microbial Cues Drive Neutrophil and Macrophage Recruitment to Thermal Injury. *iScience*. 23:101699. https://doi.org/10.1016/j.isci.2020.101699

Bortnov, V. 2020. Myeloid-Derived Growth Factor (MYDGF): Investigations of Structure and Function. The University of Wisconsin - Madison, Ann Arbor. 1–173.

Bortnov, V., D.S. Annis, F.J. Fogerty, K.T. Barretto, K.B. Turton, and D.F. Mosher. 2018. Myeloid-derived growth factor is a resident endoplasmic reticulum protein. *J. Biol. Chem.* 293:13166–13175. https://doi.org/10.1074/jbc.AC118.002052

Bortnov, V., M. Tonelli, W. Lee, Z. Lin, D.S. Annis, O.N. Demerdash, A. Bateman, J.C. Mitchell, Y. Ge, J.L. Markley, and D.F. Mosher. 2019. Solution structure of human myeloid-derived growth factor suggests a conserved function in the endoplasmic reticulum. *Nat. Commun.* 10:5612. https://doi.org/10.1038/s41467-019-13577-5

Brubaker, A.L., J.L. Rendon, L. Ramirez, M.A. Choudhry, and E.J. Kovacs. 2013. Reduced neutrophil chemotaxis and infiltration contributes to delayed resolution of cutaneous wound infection with advanced age. *J. Immunol.* 190:1746–1757. https://doi.org/10.4049/jimmunol.1201213

de Oliveira, S., E.E. Rosowski, and A. Huttenlocher. 2016. Neutrophil migration in infection and wound repair: going forward in reverse. *Nat. Rev. Immunol.* 16:378–391. https://doi.org/10.1038/nri.2016.49

Deng, Q., S.K. Yoo, P.J. Cavnar, J.M. Green, and A. Huttenlocher. 2011. Dual roles for Rac2 in neutrophil motility and active retention in zebrafish hematopoietic tissue. *Dev. Cell.* 21:735–745. https://doi.org/10.1016/j.devcel.2011.07.013

Ebaid, H. 2014. Neutrophil depletion in the early inflammatory phase delayed cutaneous wound healing in older rats: improvements due to the use of un-denatured camel whey protein. *Diagn. Pathol.* 9:46. https://doi.org/10.1186/1746-1596-9-46

Ebenhoch, R., A. Akhdar, M.R. Reboll, M. Korf-Klingebiel, P. Gupta, J. Armstrong, Y. Huang, L. Frego, I. Rybina, J. Miglietta, et al. 2019. Crystal structure and receptor-interacting residues of MYDGF - a protein mediating ischemic tissue repair. *Nat. Commun.* 10:5379. https://doi.org/10.1038/s41467-019-13343-7

Elks, P.M., F.J. van Eeden, G. Dixon, X. Wang, C.C. Reyes-Aldasoro, P.W. Ingham, M.K.B. Whyte, S.R. Walmsley, and S.A. Renshaw. 2011. Activation of hypoxia-inducible factor-1α (Hif-1α) delays inflammation resolution by reducing neutrophil apoptosis and reverse migration in a zebrafish inflammation model. *Blood.* 118:712–722. https://doi.org/10.1182/blood-2010-12-324186

Ellett, F., L. Pase, J.W. Hayman, A. Andrianopoulos, and G.J. Lieschke. 2011. mpeg1 promoter transgenes direct macrophage-lineage expression in zebrafish. *Blood.* 117:e49–e56. https://doi.org/10.1182/blood-2010-10-314120

Gagnon, J.A., E. Valen, S.B. Thyme, P. Huang, L. Akhmetova, A. Pauli, T.G. Montague, S. Zimmerman, C. Richter, and A.F. Schier. 2014. Efficient mutagenesis by Cas9 protein-mediated oligonucleotide insertion and

large-scale assessment of single-guide RNAs. *PLoS One.* 9:e98186. https://doi.org/10.1371/journal.pone.0098186

Harvie, E.A., and A. Huttenlocher. 2015. Non-invasive Imaging of the Innate Immune Response in a Zebrafish Larval Model of Streptococcus iniae Infection. *J. Vis. Exp.* 98:52788. https://doi.org/10.3791/52788

He, M., Y. Li, L. Wang, B. Guo, W. Mei, B. Zhu, J. Zhang, Y. Ding, B. Meng, L. Zhang, et al. 2020. MYDGF attenuates podocyte injury and proteinuria by activating Akt/BAD signal pathway in mice with diabetic kidney disease. *Diabetologia.* 63:1916–1931. https://doi.org/10.1007/s00125-020-05197-2

Houseright, R.A., E.E. Rosowski, P.Y. Lam, S.J.M. Tauzin, O. Mulvaney, C.N. Dewey, and A. Huttenlocher. 2020. Cell type specific gene expression profiling reveals a role for complement component C3 in neutrophil responses to tissue damage. *Sci. Rep.* 10:15716. https://doi.org/10.1038/s41598-020-72750-9

Huang, C., and P. Niethammer. 2018. Tissue Damage Signaling Is a Prerequisite for Protective Neutrophil Recruitment to Microbial Infection in Zebrafish. *Immunity.* 48:1006–1013.e6. https://doi.org/10.1016/j.immuni.2018.04.020

Huemer, K., J.M. Squirrell, R. Swader, D.C. LeBert, A. Huttenlocher, and K.W. Eliceiri. 2017. zWEDGI: Wounding and Entrapment Device for Imaging Live Zebrafish Larvae. *Zebrafish.* 14:42–50. https://doi.org/10.1089/zeb.2016.1323

Korf-Klingebiel, M., M.R. Reboll, S. Klede, T. Brod, A. Pich, F. Polten, L.C. Napp, J. Bauersachs, A. Ganser, E. Brinkmann, et al. 2015. Myeloid-derived growth factor (C19orf10) mediates cardiac repair following myocardial infarction. *Nat. Med.* 21:140–149. https://doi.org/10.1038/nm.3778

LaFave, M.C., G.K. Varshney, M. Vemulapalli, J.C. Mullikin, and S.M. Burgess. 2014. A defined zebrafish line for high-throughput genetics and genomics: NHGRI-1. *Genetics.* 198:167–170. https://doi.org/10.1534/genetics.114.166769

Livak, K.J., and T.D. Schmittgen. 2001. Analysis of relative gene expression data using real-time quantitative PCR and the 2(-Delta Delta C(T)) Method. *Methods.* 25:402–408. https://doi.org/10.1006/meth.2001.1262

Mathias, J.R., B.J. Perrin, T.X. Liu, J. Kanki, A.T. Look, and A. Huttenlocher. 2006. Resolution of inflammation by retrograde chemotaxis of neutrophils in transgenic zebrafish. *J. Leukoc. Biol.* 80:1281–1288. https://doi.org/10.1189/jlb.0506346

Maurer, L.M., B.R. Tomasini-Johansson, W. Ma, D.S. Annis, N.L. Eickstaedt, M.G. Ensenberger, K.A. Satyshur, and D.F. Mosher. 2010. Extended binding site on fibronectin for the functional upstream domain of protein F1 of Streptococcus pyogenes. *J. Biol. Chem.* 285:41087–41099. https://doi.org/10.1074/jbc.M110.153692

Miskolci, V., J. Squirrell, J. Rindy, W. Vincent, J.D. Sauer, A. Gibson, K.W. Eliceiri, and A. Huttenlocher. 2019. Distinct inflammatory and wound healing responses to complex caudal fin injuries of larval zebrafish. *eLife.* 8:e45976. https://doi.org/10.7554/eLife.45976

Montague, T.G., J.M. Cruz, J.A. Gagnon, G.M. Church, and E. Valen. 2014. CHOPCHOP: a CRISPR/Cas9 and TALEN web tool for genome editing. *Nucleic Acids Res.* 42(W1):W401-7. https://doi.org/10.1093/nar/gku410

Prasch, A.L., R.L. Tanguay, V. Mehta, W. Heideman, and R.E. Peterson. 2006. Identification of zebrafish ARNT1 homologs: 2,3,7,8-tetrachlorodibenzo-p-dioxin toxicity in the developing zebrafish requires ARNT1. *Mol. Pharmacol.* 69:776–787. https://doi.org/10.1124/mol.105.016873

Rosowski, E.E., Q. Deng, N.P. Keller, and A. Huttenlocher. 2016. Rac2 Functions in Both Neutrophils and Macrophages To Mediate Motility and Host Defense in Larval Zebrafish. *J. Immunol.* 197:4780–4790. https://doi.org/10.4049/jimmunol.1600928

Rueden, C.T., J. Schindelin, M.C. Hiner, B.E. DeZonia, A.E. Walter, E.T. Arena, and K.W. Eliceiri. 2017. ImageJ2: ImageJ for the next generation of scientific image data. *BMC Bioinformatics.* 18:529. https://doi.org/10.1186/s12859-017-1934-z

Sunagozaka, H., M. Honda, T. Yamashita, R. Nishino, H. Takatori, K. Arai, T. Yamashita, Y. Sakai, and S. Kaneko. 2011. Identification of a secretory protein c19orf10 activated in hepatocellular carcinoma. *Int. J. Cancer.* 129:1576–1585. https://doi.org/10.1002/ijc.25830

Tauzin, S., T.W. Starnes, F.B. Becker, P.Y. Lam, and A. Huttenlocher. 2014. Redox and Src family kinase signaling control leukocyte wound attraction and neutrophil reverse migration. *J. Cell Biol.* 207:589–598. https://doi.org/10.1083/jcb.201408090

The UniProt Consortium. 2017. UniProt: the universal protein knowledgebase. *Nucleic Acids Res.* 45(D1):D158–D169. https://doi.org/10.1093/nar/gkw1099

Trychta, K.A., E.J. Heathward, A. Sulima, S. Bäck, M. Farokhnia, C.T. Richie, L. Leggio, K.C. Rice, and B.K. Harvey. 2018. Extracellular esterase activity as an indicator of endoplasmic reticulum calcium depletion. *Biomarkers.* 23:756–765. https://doi.org/10.1080/1354750X.2018.1490968

Walmsley, S.R., E.R. Chilvers, A.A. Thompson, K. Vaughan, H.M. Marriott, L.C. Parker, G. Shaw, S. Parmar, M. Schneider, I. Sabroe, et al. 2011. Prolyl hydroxylase 3 (PHD3) is essential for hypoxic regulation of neutrophilic inflammation in humans and mice. *J. Clin. Invest.* 121:1053–1063. https://doi.org/10.1172/JCI43273

Wang, J., M. Hossain, A. Thanabalasuriar, M. Gunzer, C. Meininger, and P. Kubes. 2017. Visualizing the function and fate of neutrophils in sterile injury and repair. *Science.* 358:111–116. https://doi.org/10.1126/science.aam9690

Wang, Y., Y. Li, J. Feng, W. Liu, Y. Li, J. Liu, Q. Yin, H. Lian, L. Liu, and Y. Nie. 2020. Mydgf promotes Cardiomyocyte proliferation and Neonatal Heart regeneration. *Theranostics.* 10:9100–9112. https://doi.org/10.7150/thno.44281

Weiler, T., Q. Du, O. Krokhin, W. Ens, K. Standing, H. El-Gabalawy, and J.A. Wilkins. 2007. The identification and characterization of a novel protein, c19orf10, in the synovium. *Arthritis Res. Ther.* 9:R30. https://doi.org/10.1186/ar2145

Yoo, S.K., and A. Huttenlocher. 2011. Spatiotemporal photolabeling of neutrophil trafficking during inflammation in live zebrafish. *J. Leukoc. Biol.* 89:661–667. https://doi.org/10.1189/jlb.1010567

Yoo, S.K., Q. Deng, P.J. Cavnar, Y.I. Wu, K.M. Hahn, and A. Huttenlocher. 2010. Differential regulation of protrusion and polarity by PI3K during neutrophil motility in live zebrafish. *Dev. Cell.* 18:226–236. https://doi.org/10.1016/j.devcel.2009.11.015

Supplemental material

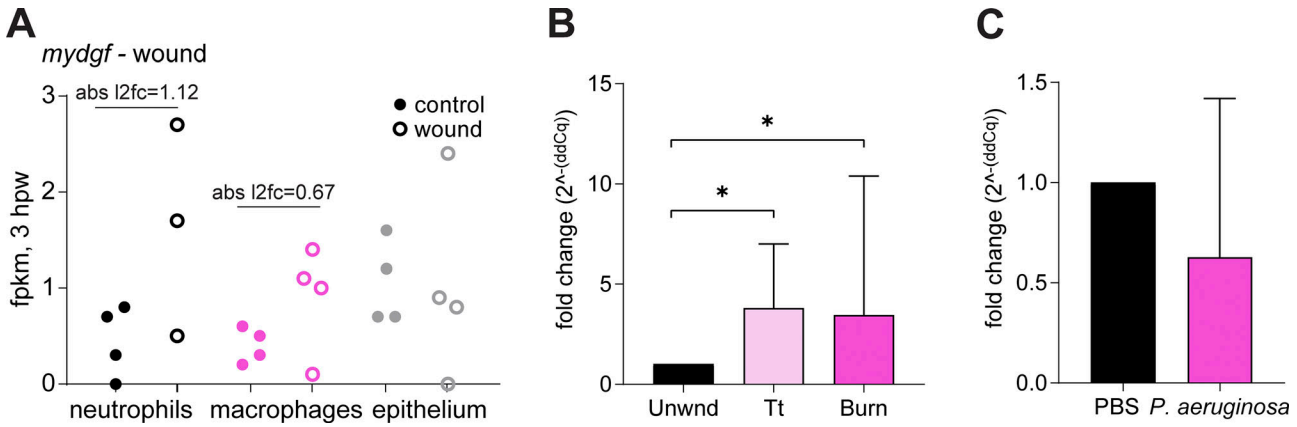

Figure S1. ***mydgf* expression in sterile injuries and infection. (A)** Expression of *mydgf*, measured by RNA sequencing (fragments per kilobase of transcript per million mapped reads [fpkm]), in three cell types is displayed 3 h following multiple wounding along the tail fin tissue. Each dot represents one independent replicate. Sample preparation and RNA-sequencing dataset was published previously (Houseright et al., 2020). **(B and C)** RT-qPCR measurement of *mydgf* expression in WT zebrafish tails 3 h following tail transection (Tt) or tail burn wound (burn; B) and *P. aeruginosa* (*Pa*; C) otic infection at 2 h after infection. Data comprise three (burn and infection) to five (Tt) independent experiments performed in technical triplicates and are normalized to *mydgf* expression in unwounded (Unwnd) tails and to *ef1α*. *n* = 50 tails per condition per independent replicate. *, P < 0.05. Fold changes in gene expression were compared with the normalized value of 1 using one-sample t tests. Data are displayed as mean with 95% CI.

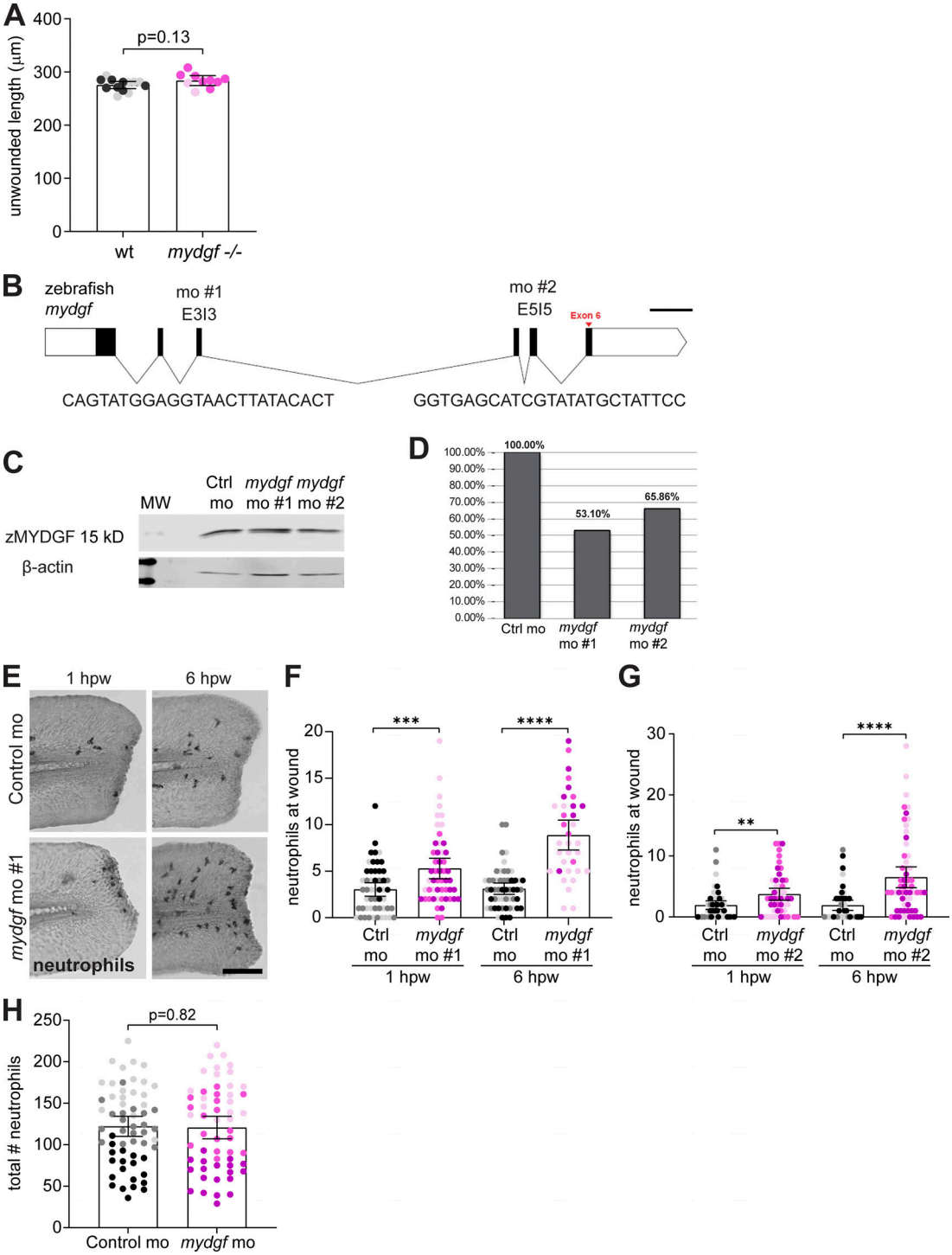

Figure S2. **Morpholino-mediated depletion of MYDGF phenocopies neutrophil accumulation at sterile injury observed in *mydgf* homozygous mutant.** **(A)** Quantification of the tail length of unwounded WT and *mydgf*$^{-/-}$ larvae at 6 dpf; two independent replicates with *n* = 13 +/+ and 10 −/−. **(B)** Schematic of zebrafish *mydgf* gene, with sequences targeted by splice-blocking morpholinos #1 and #2 highlighted at the junction of exon 3 and intron 3 and the junction of exon 5 and intron 5, respectively; scale bar = 100 bp. **(C)** Representative Western blot for zebrafish MYDGF and β-actin from pooled, 2 dpf larvae treated with either mismatch control mo or mo targeting *mydgf*. **(D)** Quantification of Western blot in C; representative of three independent replicates. **(E–G)** Representative brightfield images of Sudan Black staining (E) and quantification of the number of neutrophils in the wound microenvironment of larvae treated with either mismatch control mo and *mydgf*-targeting mo #1 (F) or mo #2 (G) at 1 and 6 hpw following tail transection of the caudal fin; three independent replicates with *n* = 52 control and 52 mo #1 at 1 hpw and 53 control and 34 mo #1 at 6 hpw (F), and three independent replicates with *n* = 47 control and 51 mo #2 at 1 hpw and 44 control and 58 mo #2 at 6 hpw (G); scale bar = 100 µm. **(H)** Quantification of the total number of neutrophils in 3 dpf whole larvae treated with mismatch control or mo #1 targeting *mgdyf*; three independent replicates with *n* = 59 control and 57 mo #1. For F–H, data are expressed as mean with 95% CI; each symbol represents one larva, and different colors represent the results of three independent replicates. ***, P < 0.001; ****, P < 0.0001. P values were calculated by ANOVA with Tukey's multiple comparisons.

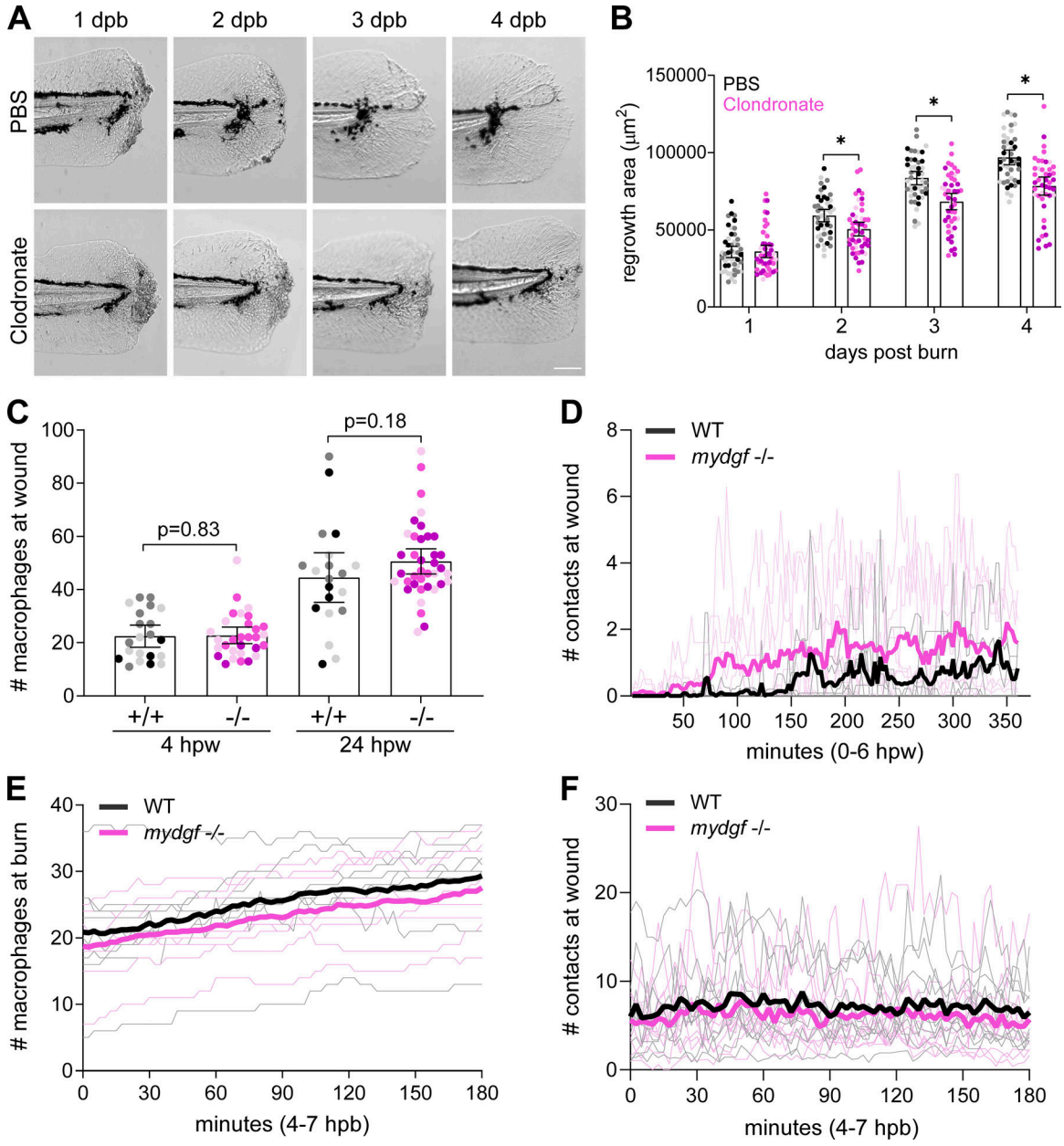

Figure S3. **Macrophage responses at sterile injuries in response to MYDGF depletion. (A and B)** Representative brightfield images (A) and quantification (B) of tail fin regrowth area following thermal injury of the caudal fin of larvae microinjected at the posterior caudal vein with PBS or clodronate liposomes (Cld); three independent replicates with *n* = 48 PBS and 49 clodronate liposomes at 1 d postburn (dpb), 47 PBS and 47 clodronate liposomes at 2 dpb, 46 PBS and 47 clodronate liposomes at 3 dpb, and 44 PBS and 45 clodronate liposomes at 4 dpb; scale bar = 100 µm. P values were calculated by unpaired two-tailed *t* test; *, P < 0.05. **(C)** Quantification of the number of macrophages at the wound microenvironment at 4 and 24 hpw following tail transection of the caudal fin of 3 dpf WT and *mydgf*$^{-/-}$ larvae; three independent replicates with *n* = 21 +/+ and 30 −/− at 4 hpw, 20 +/+ and 38 −/− at 24 hpw. P values were calculated by ANOVA with Tukey's multiple comparisons. **(D)** Quantification of the number of physical contact between neutrophils and macrophages at the wound microenvironment over the course of time-lapse imaging following tail transection of the caudal fin of 3 dpf WT and *mydgf*$^{-/-}$ larvae; four independent replicates with *n* = 7 +/+ and 11 −/− larvae; see Video 1. **(E and F)** Quantification of the number of macrophages (E) and the number of physical contacts between neutrophils and macrophages (F) at the burn microenvironment over the course of time-lapse imaging following thermal injury of the caudal fin of 3 dpf WT and *mydgf*$^{-/-}$ larvae; three independent replicates with *n* = 10 +/+ and 10 −/− larvae; see Video 2. The number of contacts displayed in D and F are adjusted values, where the raw number of contacts was multiplied by the number of neutrophils and normalized to number of macrophages at each frame. No statistical differences were detected, as calculated by unpaired two-tailed *t* test. In B and C, data are expressed as mean with 95% CI; each symbol represents one larva, and different colors represent the results of three independent replicates.

Video 1. **Neutrophil and macrophage response following tail transection of the caudal fin.** Time-lapse imaging of mCherry-labeled neutrophils and GFP-labeled macrophages at the wound microenvironment following tail transection of the caudal fin of 3 dpf WT and *mydgf*$^{-/-}$ larvae. 6-h movie showing leukocyte response at 0–6 hpw. EC Plan-NeoFluar 10×/0.30 NA, 2.5-min frame rate. Four independent replicates with n = 7 +/+ and 11 −/− larvae.

Video 2. **Neutrophil and macrophage response following thermal injury of the caudal fin.** Time-lapse imaging of mCherry-labeled neutrophils and GFP-labeled macrophages at the burn microenvironment following thermal injury of the caudal fin of 3 dpf WT and *mydgf*$^{-/-}$ larvae. 3-h movie showing leukocyte response at 4–7 hpb. Plan-Apochromat 20×/0.80 NA, 2.5-min frame rate. Three independent replicates with n = 10 +/+ and 10 −/− larvae.